energies

MDPI

Article

Characterization of Natural Gas Hydrate Constrained by Well and Seismic Data in Qiongdongnan Basin

Han Yu [1], Ju Wang [2,*], Zhangshu Lei [3], Zenggui Kuang [1], Wei Deng [1] and Lei Lu [1]

[1] Guangzhou Marine Geological Survey, China Geological Survey, Guangzhou 510700, China; kaka123614@163.com (H.Y.); kuangzenggui@mail.cgs.gov.cn (Z.K.); lulei@mail.cgs.gov.cn (L.L.)
[2] School of Computer Science, Yangtze University, Jingzhou 434000, China
[3] School of Geosciences, China University of Petroleum (Huadong), Qingdao 266580, China
* Correspondence: superjonwj@126.com

Abstract: This study investigates the natural gas hydrates within the Qiongdongnan Basin by integrating well-log and seismic data. Through pre-stack inversion and rock physics analysis, key parameters such as P-wave and S-wave impedances were utilized to distinguish hydrate-bearing formations from other geological bodies. A low-frequency model was constructed using the Inverse Distance Weighting (IDW) algorithm to improve the precision of parameter inversion. This study employs a multi-constraint inversion strategy, incorporating hard constraints from multiple wells and soft constraints from geological frameworks, ensuring reliable inversion results. Findings indicate that hydrate reservoirs are characterized by increased wave velocity and density due to hydrate accumulation, providing insights into the spatial distribution and characteristics of hydrates. This research enhances the understanding of hydrate reservoirs and offers valuable data for exploration in the Qiongdongnan Basin.

Keywords: pre-stack inversion; hydrate; rock physics analysis; reservoir prediction; Qiongdongnan

check for updates

Citation: Yu, H.; Wang, J.; Lei, Z.; Kuang, Z.; Deng, W.; Lu, L. Characterization of Natural Gas Hydrate Constrained by Well and Seismic Data in Qiongdongnan Basin. *Energies* **2024**, *17*, 5411. https://doi.org/10.3390/en17215411

Academic Editor: Ingo Pecher

Received: 18 September 2024
Revised: 22 October 2024
Accepted: 26 October 2024
Published: 30 October 2024

Copyright: © 2024 by the authors. Licensee MDPI, Basel, Switzerland. This article is an open access article distributed under the terms and conditions of the Creative Commons Attribution (CC BY) license (https://creativecommons.org/licenses/by/4.0/).

1. Introduction

Natural gas hydrates are crystalline substances that are created when water molecules and methane gas molecules combine to form a kind of ice-like, cage-shaped structures at high pressure and low temperature. Their primary habitats are the continental slope zone of marine areas that are deeper than 300 m and the permafrost zone on land [1–3]. With the increasing global energy demand, natural gas hydrates have garnered significant attention as a potential new energy source. The development of marine hydrates is crucial for addressing the future energy crisis [4]. Accurate detection, identification, and prediction of hydrate reserves have become prominent topics in current research [5,6].

Domestic and international scholars have conducted extensive research on gas hydrates in various regions. Jaiswal et al. established an accurate P-wave velocity model by integrating travel time inversion and depth migration methods to characterize the distribution of gas hydrates in the KrishnaGodavari Basin on the east coast of India [7]. Fujii et al. identified the three-dimensional structural distribution of hydrate reservoirs in the South China Sea trough near Japan through velocity analysis and seismic inversion techniques. Utilizing both 2D and 3D seismic data, along with drilling data, researchers identified over ten gas hydrate-rich areas characterized by high resistivity, strong seismic reflection, elevated P-wave velocity, and turbidite sedimentary features [8]. In the Keathley Canyon area of the Gulf of Mexico, Li et al. estimated the concentration of gas hydrates and elucidated its relationship with the bottom-simulated reflection (BSR) through a comprehensive analysis of wellbore and seismic data. By applying the modified Biot–Gassmann theory, they predicted the P-wave velocity and generated a synthetic seismogram that aligns with the three-dimensional seismic data, thereby offering significant geological and geophysical insights for the exploration and development of gas hydrates [9]. Based on the seismic data

from the Shenhu area in the northern South China Sea, Wang Xiujuan's team employed prestack inversion technology to determine the velocity and impedance characteristics of hydrates, successfully predicting their spatial distribution. This study demonstrates the effectiveness of hydrate inversion technology in elucidating three-dimensional stratigraphic structures [10].

Despite extensive research on the prediction and analysis of gas hydrate reservoirs, existing methods still face challenges in addressing complex geological structures and noise interference. Traditional post-stack inversion techniques are limited by resolution, making it difficult to effectively distinguish overlapping P-wave impedance characteristics between hydrate-bearing formations and other geological bodies [11]. In this study, a low-frequency model was constructed using the Inverse Distance Weighting algorithm, followed by adjustments to the model's weights and scaling factors to achieve more precise parameter inversion. Additionally, a multi-constraint inversion strategy was employed, integrating hard constraints from multiple wells with soft constraints from geological frameworks to enhance the stability and accuracy of the inversion results. The application of well-log-constrained inversion techniques in the Qiongdongnan Basin offers new insights for predicting hydrate reservoirs in the region. Through careful parameter optimization and advanced data processing, this approach provides a scientific foundation for the accurate assessment of gas hydrate resources, contributing to more reliable exploration and development in the area.

2. Geological Setting

The Qiongdongnan Basin is a significant oil- and gas-producing region within the deep-water basin of the South China Sea, known for its abundant hydrocarbon resources. Hydrate resources in this area are primarily concentrated in the Songnan and Lingnan highlands, as well as the Lingshui and Baodao depressions. The trial mining area in the Qiongdongnan sea region is situated southeast of Hainan Island and along the northwest edge of the northern slope of the South China Sea. This region constitutes the core of the Qiongdongnan Basin's waters. The water depth ranges from 300 m to 2600 m, encompassing an area of approximately 328 million square kilometers. The geographical location of the study area in this paper is shown in Figure 1.

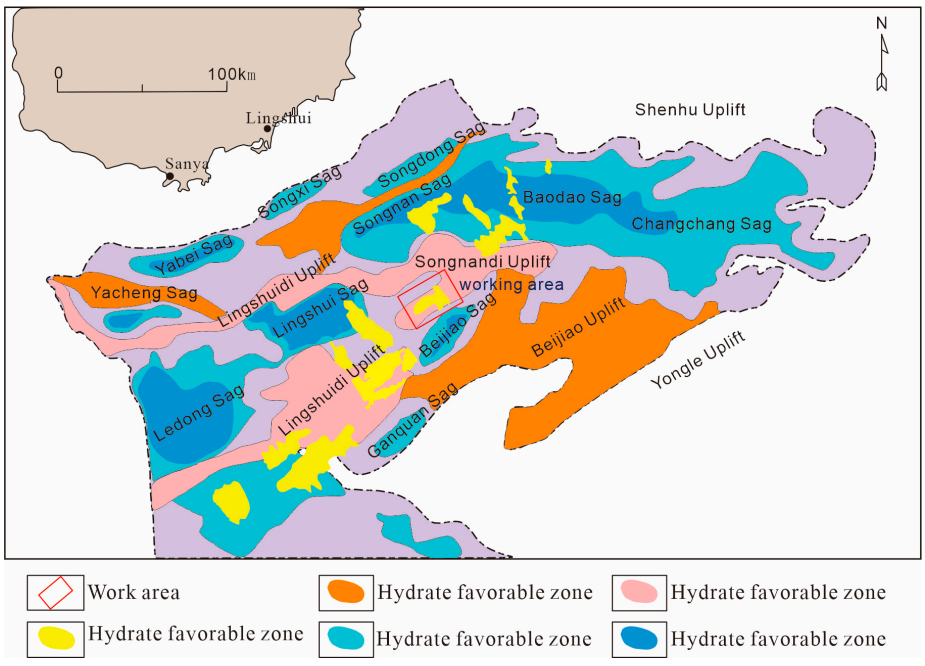


Figure 1. Geographic location map of the natural gas hydrate research area in the Qiongdongnan Sea, South China Sea.

The seabed terrain in the study area is predominantly flat, with the water depth gradually increasing from west to east, creating an overall topography that is higher in the west and lower in the east, with a gentle slope. The Qiongdongnan Sea area, situated on the Songnan Low Uplift within the Qiongdongnan Basin, has been the focus of considerable geological study. In 2018, a quasi-three-dimensional seismic survey was conducted, followed by hydrate drilling operations in both 2018 and 2019 [12].Geographically, the Qiongdongnan Basin encompasses the continental shelf and slope areas. It is bordered to the north by the uplift zone near Hainan Island, extends westward to the edge of the Yinggehai Basin, and connects to the Shenhu Ansha Uplift and Xisha Trough Basin to the east. To the south, it merges with the Xisha Islands and the Zhongjiannan Basin. Characterized by its NE-trending Cenozoic structure, the basin displays a distinctive geographic breadth—wider in the west and narrower in the east, as well as broader in the north compared to the south, with a general strike direction of NEE (approximately NE 60°). The basin is further subdivided into several secondary structural units, including the continental shelf area, slope area, central depression area, and southern fault step zone [13].

The Qiongdongnan Basin represents an offshore extension of the South China Caledonian fold belt, with a relatively thin continental shelf, ranging in thickness from 20 to 30 km. The basin's basement is predominantly composed of pre-Paleogene igneous, metamorphic, and sedimentary rocks. During the Paleogene rifting phase, the basin underwent sequential deposition of several key formations: the Eocene continental Lingtou Formation, the Lower Oligocene marine–continental transitional Yacheng Formation, and the Upper Oligocene shore–shallow marine Lingshui Formation. In the subsequent Neogene depression phase, sedimentation shifted progressively from shore–shallow marine facies to deeper marine facies, corresponding to a gradual increase in water depth. This period is marked by the deposition of several significant stratigraphic units, including the Lower Miocene Sanya Formation, the Middle Miocene Meishan Formation, the Upper Miocene Huangliu Formation, and the Pliocene Yinggehai Formation. Among these, sandstone reservoirs formed within these strata have become the primary targets for hydrocarbon exploration within the basin. The study area contains multiple wells, notably w1, w2, w3, w4, and w5. Taking w3, the thickest drilled well, as a representative example, the stratigraphy encountered includes the Lingshui, Sanya, Meishan, Huangliu, Yinggehai, and Ledong Formations. The lithological composition within these intervals consists of gray mudstone, silty mudstone, argillaceous siltstone, and grayish-white to light red granite. These lithological features provide valuable insights into the basin's depositional environment and hydrocarbon potential. Since the Upper Miocene Huangliu Formation, the region has predominantly been characterized by deep-sea plain sedimentation. The stratigraphic sequence of the Qiongdongnan Basin is shown in Figure 2.

Gene	stratum: Series	stratum: Formation	stratum: Sector	Age (Ma)	Lithological profile	Seismic profile	Lithological description	Thickness	Sedimentary facies	Construct activities	Basin filling evolution: Rifting epsiode	Basin filling evolution: By Stages
				1.64		T20	Mainly composed of light gray and green gray clay, interbedded with thin layers of silt and fine sand, rich in biological fragments, not yet diagenetic	140.2 ≀ 1318	Shallow —— Semi deep marine facies	Dongsha Activity		Post crack filling period
Neogene	Pliocene series	Yingge Huan Formation	One	2.40		T27	A large set of light gray and dark gray thick layered block shaped mudstone,Interlayer of light gray siltstone and sandy mudstone, In the central part of the basin, there are thick layers of block shaped fine sand rocks interbedded	473 ≀ 2912.5				
			Two	5.50		T30						
	Miocene series Up	Huangliu Formation		10.5		T40	Light gray to yellow gray sandstone, calcareous sandstone, biogenic limestone, Cretaceous sandstone, interbedded with varying thicknesses of calcareous mudstone	0 ≀ 664			Thermal settling curtain	
	Miocene series Middle	Meishan Formation	One	13.8		T41	Light gray mudstone interbedded with thin layers of silt and fine sandstone, which can contain calcium	0 ≀ 804	Littor facies (Shallow water platform subfacies)	South China Sea Movement		
			Two	15.5		T50	Brown, light gray powder, fine sandstone, interbedded with varying thicknesses of gray and Cretaceous rocks, as well as gray and dark gray mudstone					
	Miocene series Down	Sanya Formation	One	17.5		T52	Interbedded with gray mudstone and gray white sandstone, with block shaped mudstone at the top	0 ≀ 795				
			Two	21.0		T60	Gray dark gray mudstone, sandy mudstone, and gray white sandstone conglomerate interbedded with coal seams, with locally visible limestone at the bottom					
Paleogene	Oligocene series Up	Lingshui Formation	One	23.0		T61	Light gray gravelly sandstone, sandstone, medium to coarse sandstone, and uneven interbedded gray to dark gray mudstone	0 ≀ 368	Shore shallow sea fan delta facies	Shenhu Movement	Rift curtain	Crack filling period
			Two	25.5		T62	Mainly gray dark gray mudstone, interbedded with light gray thinlayer sandstone	0 ≀ 582				
			Three	30.0		T70	Gray white to light gray gravelly sandstone, conglomerate sandstone, medium to coarse sandstone interbedded with dark gray mudstone, with locally visible biogenic limestone	0 ≀ 730				
	Oligocene series Down	Yacheng Formation	One	32.0		T71	Gray white conglomerate, sandy conglomerate, sandstone and dark gray mud sand, interbedded with sandy mudstone, interbedded with coal seams or carbon debris	0 ≀ 910	Swamp coastal plain			
			Two	35.5		T72	Light gray and yellow gray mudstone, with thick interbedded layers of silty mudstone and light yellow gray mudstone conglomerates, medium conglomerates, etc					
			Three	36.0		T80	The upper part is interbedded with gray white sandstone and dark gray shale, with coal seams interbedded. The lower part is mainly composed of gray white and light gray conglomerates with gravel sandstone, interbedded with thin layers of deep grayColored sandy mudstone					
	Eocene series	Lingtou Formation		56.0		T100	Interbedded with light brownish red mudstone sandstone and light gray conglomerate sandstone		Lacustrine facies			
Pre-Tertiary							Granite, dolomite, tuff, volcanic agglomerate, andesite porphyrite hornfels, sedimentary rocks, mixed rocks, etc		Basement			

Figure 2. The stratigraphic sequence of the southeastern Qiong Basin [14].

3. Materials and Methods

3.1. Materials

In this study, we utilized drilling and logging data, along with two-dimensional and three-dimensional seismic data, processing techniques, and interpretation methods in the hydrate-rich region of the Qiongdongnan area in the northern South China Sea. This was further supported by an extensive review of relevant literature [15,16].

3.2. Methods

According to the data utilized, seismic inversion is categorized into two types: pre-stack inversion and post-stack inversion. The advantages of pre-stack inversion, in comparison to post-stack inversion, are primarily evident in its ability to perform three-dimensional inversions of elastic parameters, such as P-wave impedance (Zp), S-wave impedance (Zs), and density (Den), by integrating seismic data with logging data [17–21]. Unlike post-stack inversion, pre-stack inversion leverages Amplitude Versus Offset (AVO) information, which is derived from variations in the angle of incidence, to more effectively differentiate between lithology and fluid types within the reservoir. This capability enhances the accuracy of reservoir characterization. In this study, a combination of pre-stack and post-stack inversion techniques was employed based on the geological characteristics of the specific work area [22].

3.2.1. Pre-Stack Elastic Parameter Inversion

Pre-stack seismic inversion is based on the Zoeppritz equation [23,24]. Aki et al. derived an approximate expression of the P-wave reflection coefficient when the elastic difference on both sides of the interface is small [25]. This equation is widely used to invert P-wave and S-wave velocities [26]. In order to generate the amount of lithology and fluid data, it is necessary to calculate these parameters according to the relationship between sensitive elastic parameters (such as the Poisson's ratio, shear modulus, indicator factor, etc.) and rock physics research results. We further obtained the amount of lithology and fluid data, and calculated these key parameters based on the correlation between sensitive elastic parameters—the Poisson's ratio, shear modulus, indicator factors, etc.—and rock physics research. Pre-stack synchronous inversion is one of the most effective techniques for pre-stack impedance inversion [27,28].

The Aki equation can be expressed as:

$$\mathrm{R}_{pp}(\theta) = c_1 R_P + c_2 R_S + c_1 R_D \tag{1}$$

in which:

$$\mathrm{c}_1 = 1 + \tan^2\theta, R_P = \tfrac{1}{2}[\tfrac{\Delta V_P}{V_P} + \tfrac{\Delta\rho}{\rho}] \tag{2}$$

$$\mathrm{c}_2 = -8\gamma^2 \sin^2\theta, R_S = \frac{1}{2}[\frac{\Delta V_S}{V_S} + \frac{\Delta\rho}{\rho}] \tag{3}$$

$$\mathrm{c}_3 = -\frac{1}{2}\tan^2\theta + 2\gamma^2\sin^2\theta, R_D = \frac{\Delta\rho}{\rho}, \gamma = \frac{V_S}{V_P} \tag{4}$$

$$\rho = \frac{\rho_2 + \rho_1}{2}, V_P = \frac{V_{P2} + V_{P1}}{2}, V_S = \frac{V_{S2} + V_{S1}}{2} \tag{5}$$

$$\Delta\rho = \rho_2 - \rho_1, \Delta V_P = V_{P2} - V_{P1} \tag{6}$$

$$\Delta V_S = V_{S2} - V_{S1}, \theta = \frac{\theta_i + \theta_t}{2} \tag{7}$$

Here, θ, ρ_1, ρ_2, V_{P1}, V_{P2}, V_{S1}, and V_{S2} represent the incident angle and the density (Den) of the upper and lower layers, as well as the P-wave and S-wave velocities of the upper and lower interfaces. Considering the presence of water-bearing formations, the following trends can be observed.

By $\frac{V_s}{V_p} = \theta = constant$, it can be concluded:

$$\ln(Z_s) = \ln(Z_p) + \ln(\theta) \tag{8}$$

By $\rho = aV_P^b$,

$$\ln(\rho) = \frac{b}{1+b}\ln(Z_p) + \frac{\ln(a)}{1+b} \tag{9}$$

From the aforementioned relationship, a more general trend can be established.

$$\ln(Z_s) = k\ln(Z_p) + kC + \Delta L_s \tag{10}$$

$$\ln(\rho) = m\ln(Z_p) + mC + \Delta L_D \tag{11}$$

Thus, the Fatti equation is derived.

$$T(\theta) = \widetilde{C_1}W(\theta)DL_p + \widetilde{C_2}D\Delta L_s + \widetilde{C_3}W(\theta)D\Delta L_D \tag{12}$$

qorum: $\widetilde{C_1} = C_1 + \frac{1}{2}kC_2 + mC_3$, $\widetilde{C_2} = \frac{1}{2}C_2$, and $W(\theta)$ represents the wavelet corresponding to the incident angle, while D denotes the derivative factor $L_P = \ln(Z_p)$.

The equation establishes the relationship between the physical characteristics of regional rocks and the various variables under the geological conditions of the aquifer. The wavelet can effectively balance the differences in amplitude among the partial superposition data collected at different angles, resulting in more accurate outcomes.

In calculating elastic parameters, we inverted the P-wave impedance (Zp) and S-wave impedance (Zs) using the Zoeppritz equation. We then calculated the Poisson's ratio and shear modulus to aid in distinguishing the lithology and fluid characteristics of the reservoir. To enhance the stability of the inversion results, we implemented a strategy that combines soft and hard constraints. Soft constraints regulate the continuity of the model by considering the lateral variations in seismic data, while hard constraints utilize well data and a geological structural framework model to ensure the accuracy of longitudinal changes.

3.2.2. Rock Physics Analysis Techniques

Logging rock physical analysis serves as the foundation for seismic reservoir prediction research. This analysis provides detailed information about the physical properties of reservoir rocks, which is crucial for conducting environmental corrections, reconstructing abnormal curves, and standardizing data processing [29–31]. Such procedures ensure the accuracy and comparability of logging data, enhancing its reliability compared to drilling data. The reinterpretation of logging data aids in revealing the relationships between oil and gas reservoirs, lithology, and fluid configurations. It also assesses whether the elastic parameters of the rocks can effectively distinguish hydrocarbon-bearing reservoirs in the target area, thereby offering robust support for accurately identifying reservoir characteristics and facilitating oil and gas exploration and development [32].

3.2.3. Construction of Low-Frequency Model

In well-log-constrained seismic inversion, the construction of a low-frequency model plays a crucial role in determining the quality of the final inversion results. We employed the Inverse Distance Weighting (IDW) interpolation algorithm to build the low-frequency model [33]. In this algorithm, each sampling point contributes to the interpolated value with a specific weight, which decreases as the distance between the sampling point and the interpolation point increases. Therefore, points closer to the interpolation target carry greater weight in the calculation. The IDW algorithm involves performing a weighted average by first determining the weights for all sample points. Each sample value is then multiplied by its corresponding weight, and the products are summed to obtain a total value. This total is subsequently divided by the sum of all weights to compute the final

interpolated value. This method ensures that points near the interpolation location have a more significant influence, improving the stability and accuracy of the low-frequency model, which is essential for enhancing the reliability of seismic inversion results.

$$Z_p = \sum_{i=1}^{n} (d_i^{-u} \times Z_i) / \sum_{i=1}^{n} d_i^{-u} \tag{13}$$

In the interpolation formula, Zp represents the elevation value at the interpolation point, di denotes the distance from the i sampling point to the interpolation point, and di-u serves as the distance decay function. The weight exponent u controls how the influence of other points diminishes as the distance increases, ensuring that the contribution of more distant points decreases accordingly.We constructed low-frequency models for similar regions, with the interpolation algorithm and the selection of individual well weights being critical factors in the modeling process. The well distribution of similar regions is shown in Figure 3.In these regions, hydrate and free gas coexist within the same sand layer and exhibit lateral distribution patterns. However, with only a single well penetrating the gas-bearing layer and sparse spatial constraints, it becomes essential to carefully determine the influence range and weight of each well. The weight of each well in the study area is shown in Figure 4.The appropriate selection of these parameters ensures the reliability and accuracy of the model, especially under limited spatial data conditions.

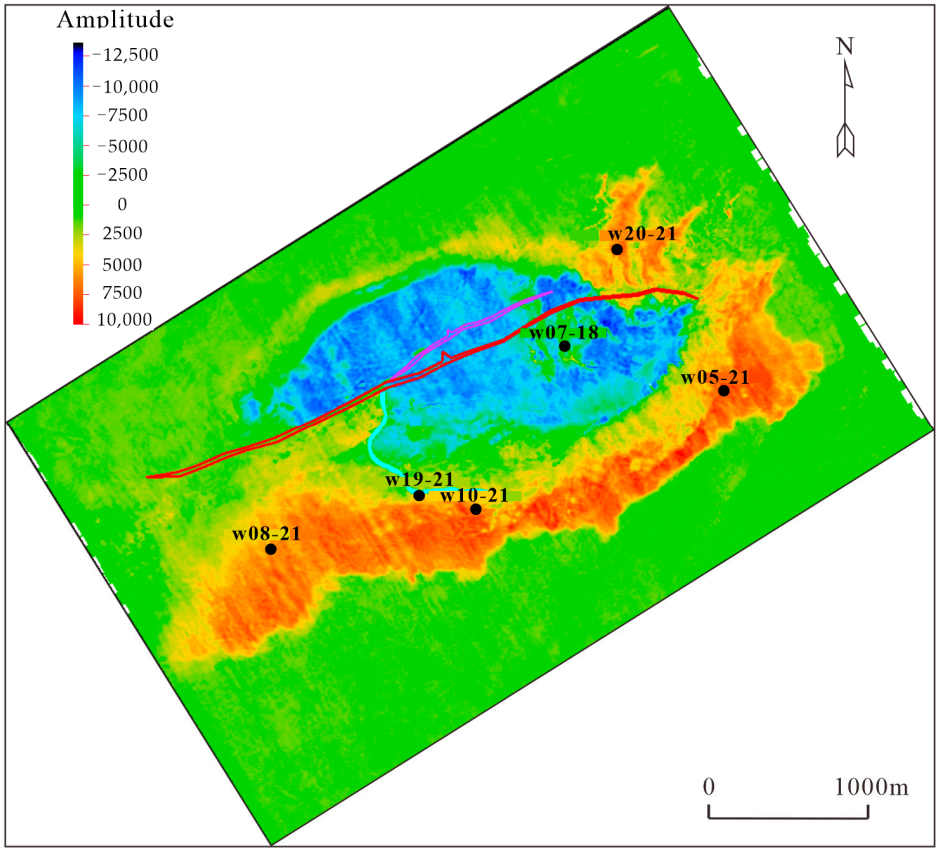


Figure 3. Well location distribution in similar areas [5].

In this study, the global kriging algorithm was applied to control the influence radius of individual wells. Given the good connectivity of the sandstone reservoirs, the influence range for these wells corresponds to the distribution radius of the gas-bearing layer. For well W07-18, the same principle applies; however, since a greater number of wells penetrate the hydrate-bearing layers, the constraint radius for each well in the hydrate layers is smaller

than that of W07-18. This approach ensures that the influence radius reflects the specific geological conditions, improving the reliability and precision of the inversion results.

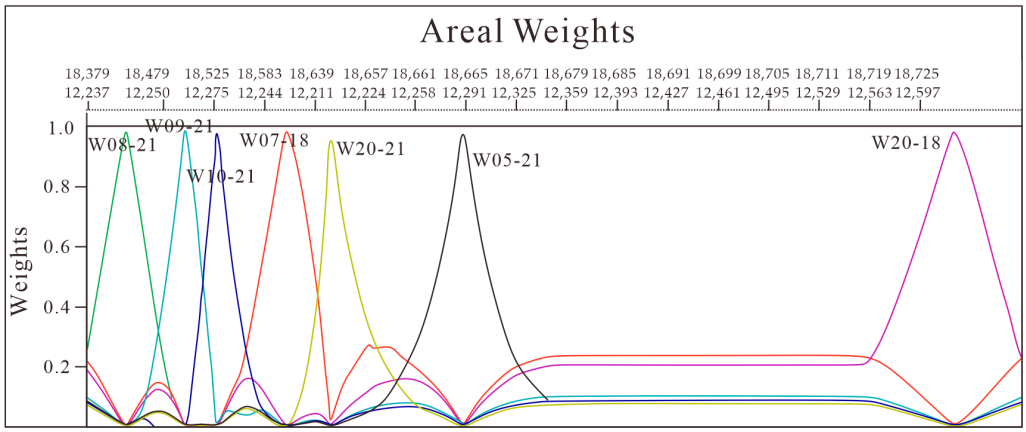


Figure 4. Spatial weight distribution of a single well.

Figure 5 presents the low-frequency model constructed from correlated wells, illustrating how the model aligns with geological patterns. The model shows good agreement with well-log data at well locations, accurately distinguishing between hydrate-bearing layers and free gas layers. This separation ensures a reliable low-frequency background trend, which serves as a solid foundation for subsequent inversion processes. The coherence between the low-frequency model and the geological structure enhances the robustness and accuracy of the inversion results, facilitating more precise reservoir characterization.

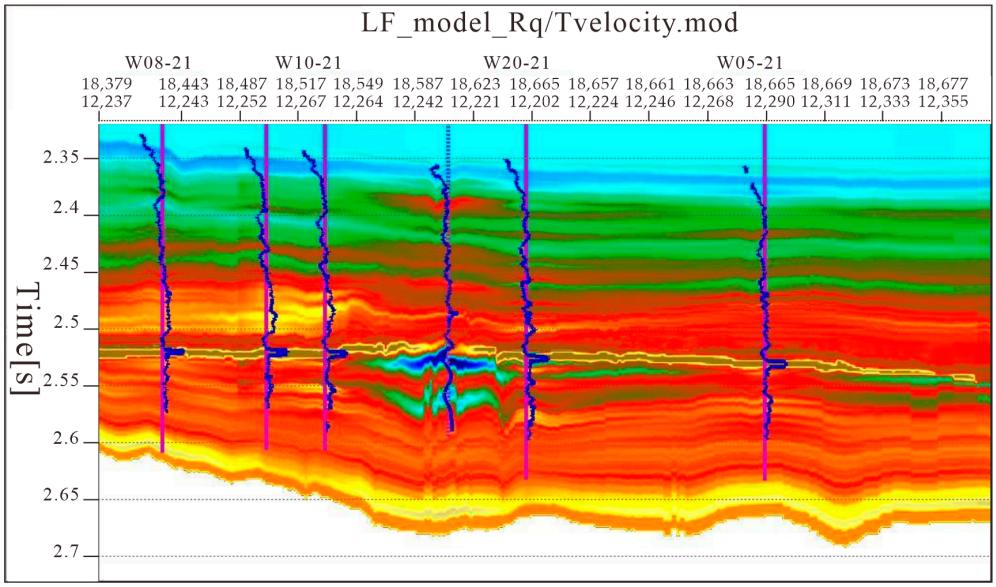


Figure 5. Low-frequency model of similar regions.

4. Results

4.1. Rock Physics Characteristics

Using the standardized well-log data, we conducted rock physics analysis, focusing first on the differences between the predicted and original log data. Figure 6 presents a comparison of the intersection plots of velocity and density before and after prediction. As shown in Figure 6a, the P-wave velocities in the range of 1500 m/s to 1900 m/s exhibit a scattered and intertwined pattern between hydrate-bearing and non-hydrate formations, making them difficult to distinguish. In contrast, Figure 6b demonstrates that, after forward modeling, the boundaries between hydrate-bearing and non-hydrate formations become

clearer, resulting in better differentiation. The post-simulation well-log curves exhibit more distinct patterns, justifying the use of these corrected curves for subsequent rock physics analysis.

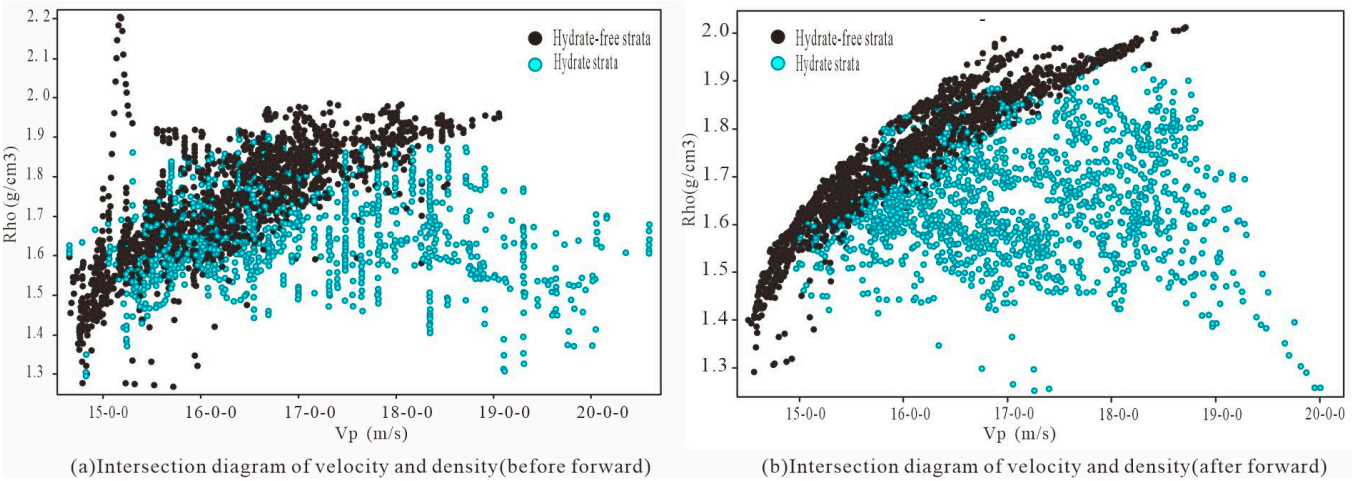


Figure 6. Comparison of velocity and density intersection before and after formation forward modeling.

Figure 7 presents an analysis of the intersection diagram depicting the elastic parameters associated with hydrate formation. It is evident that the hydrate formation and non-hydrate formation are intertwined in the intersection diagram of the individual elastic parameters, making it difficult to clearly distinguish between the two. However, by examining the intersection of multiple parameters, more accurate results can be achieved. Specifically, when the longitudinal wave velocity (Vp) exceeds 1700 m/s and the density ranges from 1.25 to 1.75, the intersection of Vp and density demonstrates the most effective recognition of hydrates. Consequently, Vp and density were primarily selected for the identification of hydrates.

To further analyze the petrophysical characteristics of different hydrate saturations, hydrates were identified on the logs, which is based on the results of the intersection of longitudinal wave velocity and density. As shown in Figure 8, the identified hydrates are in good agreement with the results of log interpretation.

Based on the above analysis, the natural gas hydrates in this region exhibit the following characteristics. As shown in Figure 8, within the 1700 m-to-1900 m depth range, areas with higher P-wave velocities correspond to low-density hydrate zones, aligning well with the well-log interpretation results. The P-wave impedance of the gas hydrates significantly overlaps with that of the surrounding sedimentary formations, making post-stack impedance ineffective in distinguishing between hydrate and non-hydrate layers. Therefore, it is essential to apply pre-stack elastic parameter inversion for more accurate identification of gas hydrates. Rock physics analysis using predicted P-wave and S-wave velocities reveals more distinct patterns compared to the original data. The intersection of P-wave velocity and density provides a useful method for identifying hydrates. Additionally, there is a positive correlation between hydrate saturation and P-wave velocity, indicating that the P-wave velocity can reflect the saturation level of the hydrates. According to the rock physics analysis, Figure 8 shows that the density and resistivity profiles from the three wells correspond closely to the characteristics of a pore-filling hydrate model. This suggests that the hydrates in this area primarily follow a pore-filling pattern, and the predicted P-wave and S-wave velocities based on this model align well with the observed trends in the measured data [4,34].

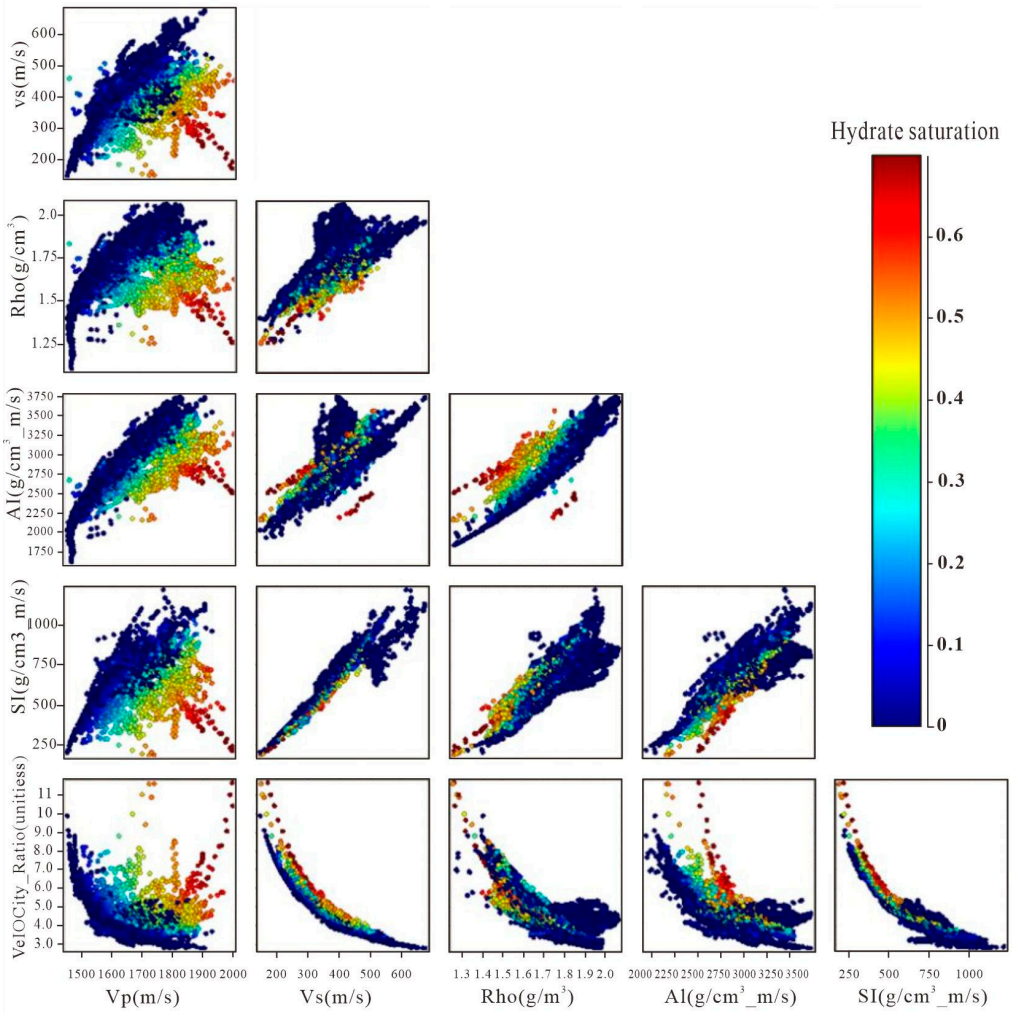


Figure 7. Analysis of elastic parameter intersection diagram.

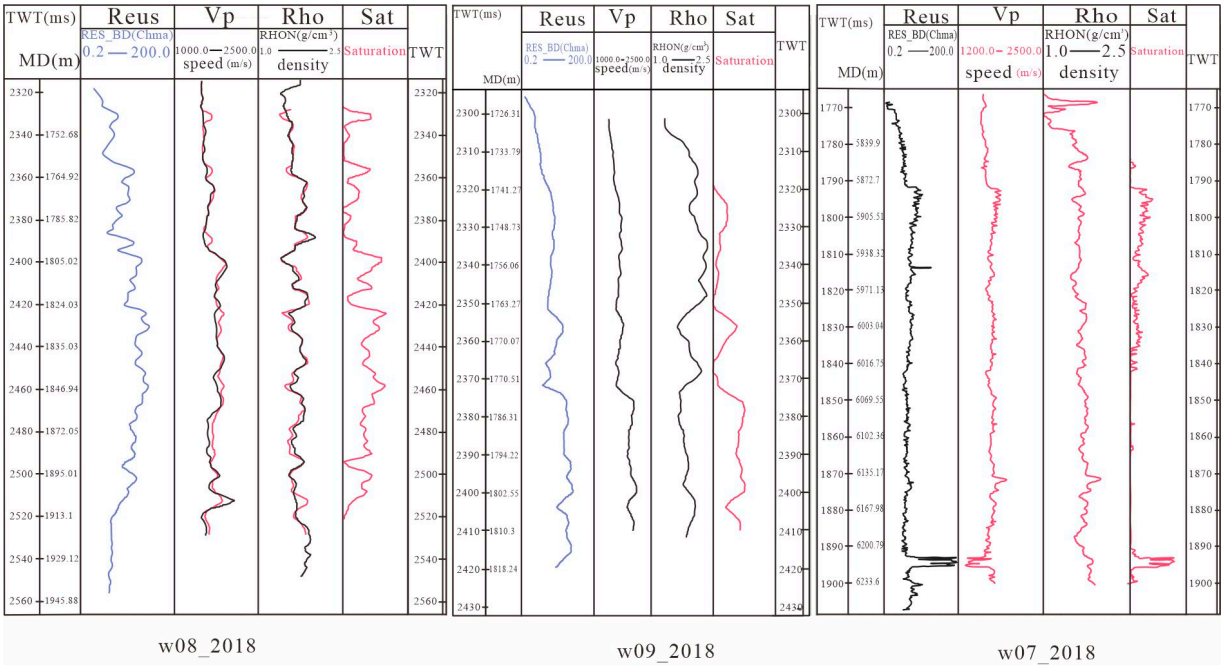


Figure 8. Identification of hydrates by intersection of P-wave velocity (VP) and density.

4.2. Synthetic Seismic Record Calibration

The calibration of synthetic records is a crucial step in reservoir inversion, as the calibration results directly influence the accuracy of the inversion outcomes. Through meticulous calibration, a more precise time-depth relationship and seismic wavelet can be obtained. This detailed calibration of the reservoir is divided into three steps: First, a Ricker wavelet is employed for preliminary calibration, during which several marker layers across the entire area—such as the seabed and the top and bottom interfaces of the natural gas hydrate layer—are calibrated. On the basis of preliminary calibration, the best statistical wavelet is extracted by using the well-side seismic trace and well curve, and the synthetic seismic record is re-made by using the wavelet, and the time-depth relationship is continuously corrected to make the synthetic seismic record and the well-side seismic best match. Through the extraction and analysis of the best wavelet in each well, the comprehensive wavelet in the working area is finally determined, and the target horizon is calibrated. The W6 well, W7 well, and W8 well in the work area were calibrated, and the results are shown in Figure 9.

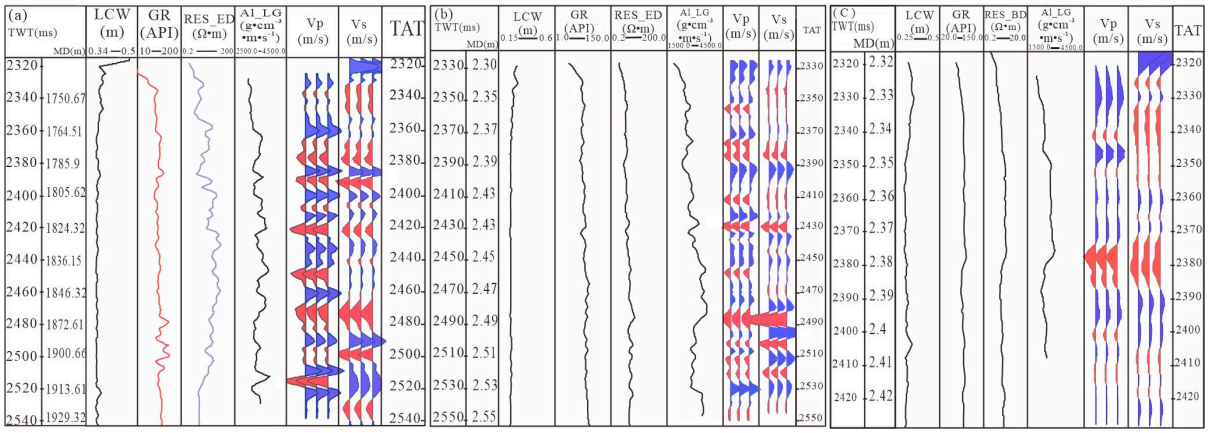


Figure 9. Results of synthetic seismic record calibration.

High correlation is observed in the calibration findings of the synthesized well-logging data within the working region. However, three wells—W7, W8, and W9—exhibit relatively low correlations, with correlation values ranging from 0.5 to 0.6. The seismic wavelet is shown in Figure 10.

After completing the post-stack calibration, it is also essential to calibrate the angle stack. This calibration primarily aims to obtain the angle-divided seismic wavelet. We define the incident angle range as between 0° and 40°, which is further divided into three segments: 0–15°, 16–25°, and 26–40°. Although the data within the 0–15° and 16–25° ranges exhibit high levels of noise, they are beneficial for achieving stable inversion results. Conversely, while the signal-to-noise ratio in the 26–40° range is low, it provides additional stratigraphic information, enhancing the completeness of the inversion results. The angle calibration results for the W6 well are illustrated in Figure 8. The calibration outcomes are more favorable for the 0–15° and 16–25° stacks, whereas the results for the 26–40° stacks are less satisfactory, primarily due to a reduction in the far-field signal-to-noise ratio. Figure 11 presents seismic wavelets extracted across different angles, from near-offset to far-offset stacks. As the offset increases, noise interference becomes more pronounced, resulting in noticeable changes in the wavelet shape. The wavelets extracted from far-offset data are more significantly affected by noise. To mitigate these effects, we applied a stacking and averaging approach within the same offset range to enhance the signal-to-noise ratio (SNR). This method effectively reduces random noise in the far-offset data, ensuring more reliable seismic wavelets for further analysis. The angle stack seismic wavelet of well W6 is shown in Figure 12.

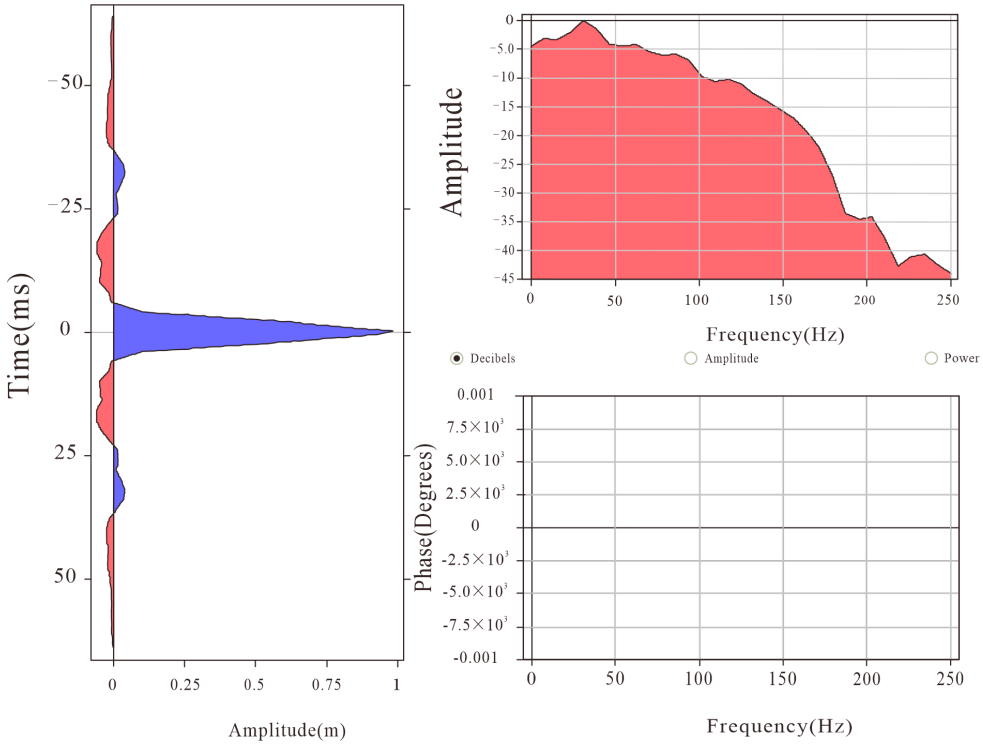


Figure 10. Seismic wavelet.

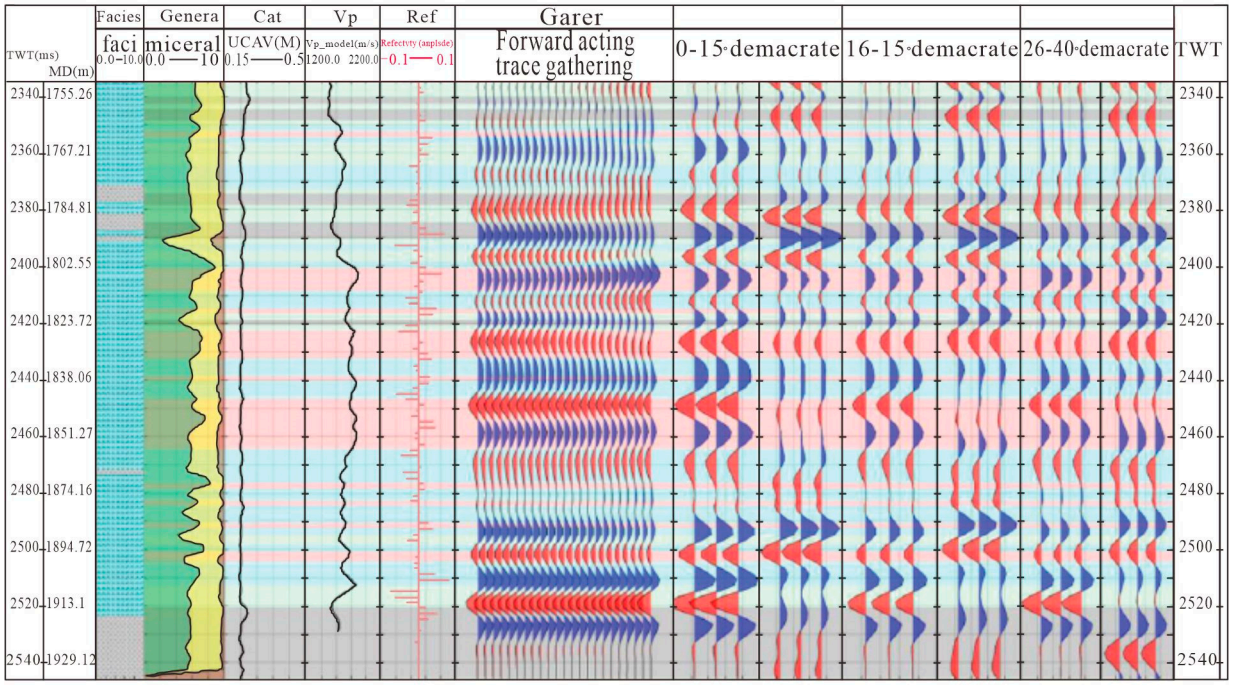


Figure 11. The angle–domain calibration results for Well W6.

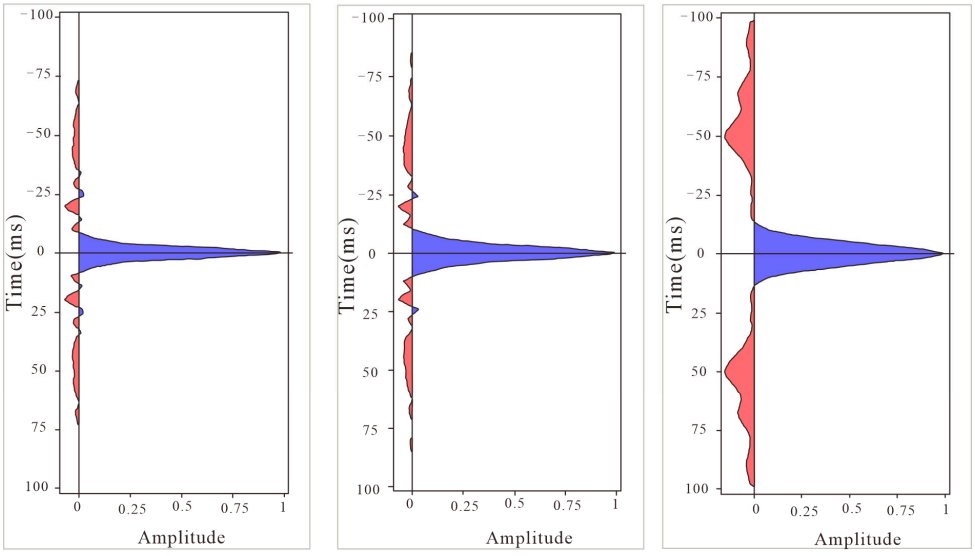


Figure 12. The seismic waveforms of angle–domain stacking for Well W6.

4.3. Prediction of Rock Physics Inversion Results

On the basis of establishing a reasonable low-frequency model and extracting high-quality wavelets, after selecting appropriate inversion parameters, we set the model weight and scale factor to between 0.6 and 1.2 in the process of inversion model construction, so that the scale factor could be adjusted through the statistical analysis of well-side data. We then reduced the error between different wells. The filtering parameters were processed by 10–80 Hz band-pass filtering, which can not only effectively reduce noise interference but also ensure that the key information of the target layer is not lost. Prestack simultaneous inversion can then be performed. In the inversion process, the wave impedance trend hard constraint of multiple wells, the geological structure framework model, and the seismic data soft constraint are added. The soft constraint mainly controls the lateral change, and the logging data hard constraint controls the longitudinal change. According to the results of rock physics analysis, the P-velocity, density, and wave impedance inversion results were selected for analysis. The results are shown in Figures 13 and 14.

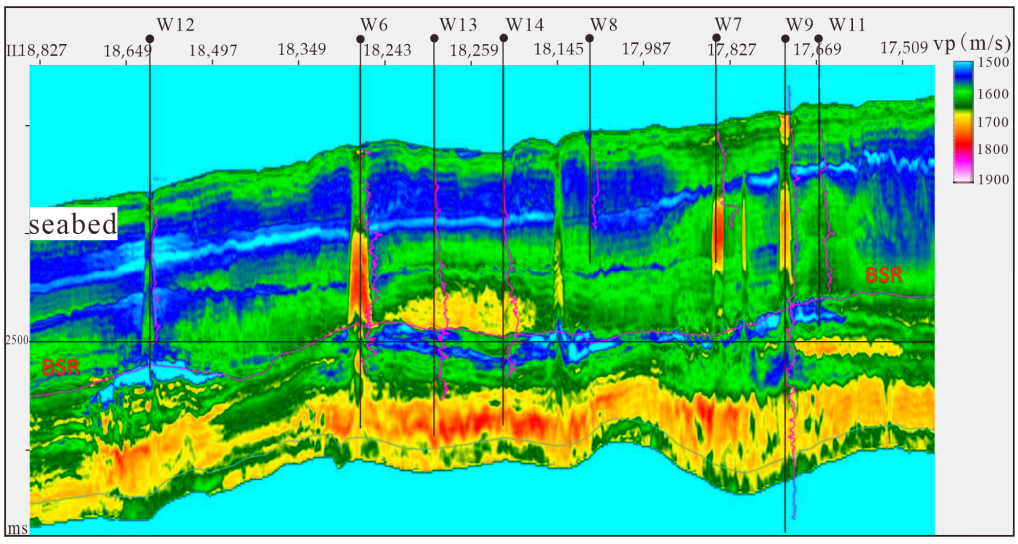


Figure 13. Inversion of the longitudinal wave velocity profile along the well trajectory.

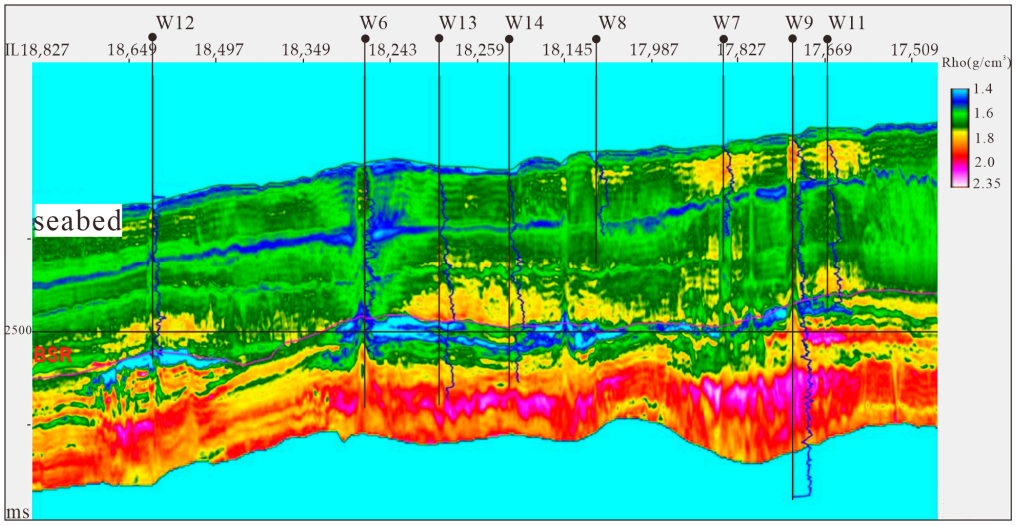


Figure 14. Inversion of the density profile along the well trajectory.

5. Discussion

Through rock physics analysis and synthetic seismic record calibration in this study, we have gained a comprehensive understanding of the characteristics of natural gas hydrates in southeastern Hainan. Since the correlation between saturation and impedance is not as strong as that between velocity and saturation, it is essential to utilize pre-stack seismic inversion velocities to calculate saturation, density, and porosity. According to our rock physics analysis, the formation becomes denser and more rigid due to hydrate filling. Following hydrate accumulation, the P-wave velocity typically increases significantly, ranging from 1500 m/s to between 2100 m/s and 4000 m/s, or even higher. It is believed that the hydrates in the study area are primarily characterized by a pore-filling mode [34,35]. The predicted P-wave and S-wave velocities align well with the measured data. When compared to the original data, the trends become more pronounced by employing the optimized predicted logging curve for rock physics analysis. Notably, the joint analysis of P-wave velocity and density intersections can more accurately identify hydrates, and there exists a correlation between hydrate saturation and P-wave velocity, which can serve as an index to effectively reflect hydrate saturation.

In this study, precise calibration of synthetic seismic records was performed to obtain accurate time–depth relationships and seismic wavelets. The calibration results indicate that most wells within the study area exhibited high correlation between synthetic and recorded seismic data. However, some wells showed relatively lower correlation, which may be attributed to the complexity of geological structures.

For rock physics-based inversion predictions, key parameters such as velocity, density, and acoustic impedance were selected for analysis. By incorporating appropriate inversion parameters and applying hard constraints from multiple wells along with soft constraints from geological framework models, reliable inversion results were achieved. These results provide valuable insights for further investigation into the distribution and characteristics of natural gas hydrates in the region. This research integrates well-log and seismic data, employing precise model-building methods and meticulous parameter optimization strategies [36]. Such an approach enhances the exploration of hydrate reservoirs in the Qiongdongnan Basin, advancing the understanding of gas hydrate resources in this area.

6. Conclusions

(1) P-impedance was conducted to establish the seismic sub-wave and time–depth relationship. Based on this relationship, sub-angle stacking calibration was performed, yielding a strong correlation in the calibration results.

(2) A reliable low-frequency model was established by integrating stratigraphic horizons, well-log data, and velocity data using the Inverse Distance Weighting (IDW) algorithm. The resulting model aligns well with the geological features and provides a robust foundation for further seismic inversion.
(3) The model weights, scale factors, and filtering parameters are optimized, and pre-stack simultaneous inversion is performed. The inversion results clearly indicate the presence of hydrates.

Author Contributions: Conceptualization, H.Y. and J.W.; methodology, H.Y. and W.D.; software, J.W. and Z.L.; validation, H.Y., Z.L., L.L. and J.W.; resources, W.D. and L.L.; data curation, H.Y. and L.L.; writing—original draft preparation, H.Y.; writing—review and editing, Z.K.; visualization, J.W. and Z.L.; supervision, W.D. and Z.K. All authors have read and agreed to the published version of the manuscript.

Funding: The research works are financially supported by the National Key Research and Development Program of China (No. 2021YFC2800901). This study was funded by the Guangzhou Basic and Applied Basic Research Foundation (grant No. 202201011106) and the Guangdong Major Project of Basic and Applied Basic Research (2020B0301030003).

Data Availability Statement: In compliance with confidentiality agreements related to the data used in this scientific paper, specific details and figures cannot be disclosed publicly. We ensure that all sensitive information is handled with the utmost confidentiality and is used solely for the purposes of this research. We appreciate the understanding and cooperation of all parties involved in adhering to these confidentiality requirements.

Conflicts of Interest: The authors declare no conflicts of interest.

References

1. Moridis, G. Toward Production From Gas Hydrates: Current Status, Assessment of Resources, and Simulation-Based Evaluation of Technology and Potential. *Lawrence Berkeley Natl. Lab.* **2008**, *12*, 30–71. [CrossRef]
2. Makogon, Y.F.; Holditch, S.A.; Makogon, T.Y. Natural Gas Hydrates—A Potential Energy Source for the 21st Century. *J. Pet. Sci. Eng.* **2007**, *56*, 14–31. [CrossRef]
3. Farahani, M.V.; Hassanpouryouzband, A.; Yang, J.; Tohidi, B. Development of a Coupled Geophysical–Geothermal Scheme for Quantification of Hydrates in Gas Hydrate-Bearing Permafrost Sediments. *Phys. Chem. Chem. Phys.* **2021**, *23*, 24249–24264. [CrossRef] [PubMed]
4. Farahani, M.V.; Hassanpouryouzband, A.; Yang, J.; Tohidi, B. Insights into the Climate-Driven Evolution of Gas Hydrate-Bearing Permafrost Sediments: Implications for Environmental Impact Prediction and Energy Security. *RSC Adv.* **2021**, *11*, 14334–14346. [CrossRef] [PubMed]
5. Kuang, Z.; Cook, A.; Ren, J.; Deng, W.; Cao, Y.; Cai, H. A Flat-Lying Transitional Free Gas to Gas Hydrate System in a Sand Layer in the Qiongdongnan Basin of the South China Sea. *Geophys. Res. Lett.* **2023**, *50*, e2023GL105744. [CrossRef]
6. Collett, T.; Johnson, A.; Knapp, C.; Boswell, R. *Natural Gas Hydrates—Energy Resource Potential and Associated Geologic Hazards*; AAPG Memoir: Tulsa, OK, USA, 2009; p. 89.
7. Jaiswal, P.; Dewangan, P.; Ramprasad, T.; Zelt, C.A. Seismic Characterization of Hydrates in Faulted, Fine-Grained Sediments of Krishna-Godavari Basin: Unified Imaging. *J. Geophys. Res. Solid Earth* **2012**, *117*, B4. [CrossRef]
8. Kobayashi, T.; Inamori, T.; Hayashi, M.; Takano, O.; Yokoi, K. Resource Assessment of Methane Hydrate in the Eastern Nankai Trough, Japan. In Proceedings of the Offshore Technology Conference, Houston, TX, USA, 5–8 May 2008. [CrossRef]
9. Lee, M.W.; Collett, T.S. Integrated Analysis of Well Logs and Seismic Data to Estimate Gas Hydrate Concentrations at Keathley Canyon, Gulf of Mexico. *Mar. Pet. Geol.* **2008**, *25*, 924–931. [CrossRef]
10. Wang, X.; Wu, S.; Liu, X.; Yang, S.; Guo, Y.; Li, Q. Estimation of Gas Hydrates Resources Based on Well Log Data and Seismic Data in Shenhu Area. *Prog. Geophys.* **2010**, *25*, 1288–1297.
11. Guo, P.; Zhang, S.; Zhang, G.; Zhong, Q. Application of Prestack Joint Inversion of P- and S-Waves. *Oil Geophys. Prospect.* **2013**, *48*, 53–57.
12. Fu, X.; Zhang, F.; Li, X.; Qian, Z.; Chen, H.; Mei, L. Simultaneous Inversion of P- and S-Wave Impedances Based on an Improved Approximation Equation of Reflection Coefficients. *Chin. J. Geophys.* **2019**, *62*, 276–288.
13. Yu, X.; Wang, J.; Liang, J.; Li, S.; Zeng, X.; Li, W. Depositional Characteristics and Accumulation Model of Gas Hydrates in Northern South China Sea. *Mar. Pet. Geol.* **2014**, *56*, 74–86. [CrossRef]
14. Xie, W.; Zhang, Y.; Sun, Z.; Jiang, J. Characteristics and Formation Mechanism of Faults in Qiongdongnan Basin. *Mar. Geol. Quat. Geol.* **2007**, *27*, 71–78.

15. He, J.; Ning, Z.; Zhao, B.; Wan, Z.; Meng, D. Preliminary Analysis and Prediction of Strategic Replacement Area for Gas Hydrate Exploration in South China Sea. *Earth Sci.* **2022**, *47*, 1549–1568.
16. He, Y.; Liang, J.; Shi, W.; Kuang, Z.; Deng, W.; Wang, R.; Xu, L.; Du, H. Influencing Factors and Accumulation Modes of Gas Hydrate in South Low Uplift and Its Surrounding Area of Qiongdongnan Basin. *Earth Sci. -J. China Univ. Geosci.* **2022**, *47*, 1711–1727.
17. Yang, P.; Yin, X. Non-linear Quadratic Programming Bayesian Prestack Inversion. *Chin. J. Geophys.* **2008**, *51*, 1876–1882.
18. Gray, D.; Goodway, B.; Chen, T. Bridging the Gap: Using AVO to Detect Changes in Fundamental Elastic Constants. *SEG Tech. Program Expand. Abstr.* **1999**, *1999*, 852–855.
19. Connolly, P. Elastic Impedance. *Lead. Edge* **1999**, *18*, 438–452. [CrossRef]
20. Yu, X.; Zhang, Z.; Su, X.; Chen, F.; Li, Y. Primary Discussion on Accumulation Conditions for Sedimentation of Gas Hydrate and Its Distribution in South China Sea. *Earth Sci. Front.* **2004**, *11*, 311–315.
21. Hilterman, F.J. Is AVO the Seismic Signature of Rock Properties? *SEG Tech. Program Expand. Abstr.* **1989**, *1989*, 559.
22. Whitcombe, D.N.; Connolly, P.A.; Reagan, R.L.; Redshaw, T.C. Extended Elastic Impedance for Fluid and Lithology Prediction. *Geophysics* **2002**, *67*, 63–67. [CrossRef]
23. Yang, S.; Zhou, X. Series Expression and Approximation of Zoeppritz's Equation. *Oil Geophys. Prospect.* **1994**, *29*, 399–412.
24. Aik, K.; Richards, P.G. Quantitative Seismology: Theory and Methods. *San Fr. Freeman* **1980**, *1*, 557.
25. Fatti, J.L.; Smith, G.C.; Vail, P.J.; Strauss, P.J.; Levitt, P.R. Detection of Gas in Sandstone Reservoirs Using AVO Analysis: A 3-D Seismic Case History Using the Geostack Technique. *Geophysics* **1994**, *59*, 1320–1465. [CrossRef]
26. Zong, Z.; Yin, X.; Wu, G. AVO Inversion and Poroelasticity with P- and S-Wave Moduli. *Geophys. J. Soc. Explor. Geophys.* **2012**, *77*, N17–N24. [CrossRef]
27. Li, L.; Lei, X.; Zhang, X.; Sha, Z. Gas Hydrate and Associated Free Gas in the Dongsha Area of Northern South China Sea. *Mar. Pet. Geol.* **2013**, *39*, 92–101. [CrossRef]
28. Luo, S.; Zhang, L.; Zhao, Y.; Deng, W.; Lei, Z.; Shuai, Q. "Application of Extended Elastic Impedance Based Petrophysical Analysis Technique in Oil-Gas Bearing Detection in Beikang Basin. " *Comput. Tech. Geophys. Geochem. Explor.* **2021**, *43*, 331–339.
29. Liu, W.; Du, W.; Guo, Y.; Li, D. Lithology Prediction Method of Coal-Bearing Reservoir Based on Stochastic Seismic Inversion and Bayesian Classification: A Case Study on Ordos Basin. *J. Geophys. Eng.* **2022**, *19*, 494–510. [CrossRef]
30. Xu, H.; Yang, S.; Zheng, X.; Wang, M.; Wang, J. Seismic Identification of Gas Hydrate and Its Distribution in Shenhu Area, South China Sea. *Chin. J. Geophys.* **2010**, *53*, 1691–1698.
31. Ecker, C.; Dvorkin, J.; Nur, A.M. Estimating the Amount of Gas Hydrate and Free Gas from Marine Seismic Data. *GeoSci.-World* **2010**, *31*, 29. [CrossRef]
32. Qian, J.; Wang, X.; Dong, D.; Sain, K.; Ye, Y. New Estimation of Anisotropic Saturation and Fracture Quantitative Evaluation for Fracture-Filling Gas Hydrate Reservoir. *Prog. Geophys.* **2019**, *34*, 354–364.
33. Wang, K.; Gao, L.; Jiang, F. A Method of Seabed DEM Modeling Based on the Improved Inverse Distance Weighted Interpolation Algorithm. *Hydrogr. Surv. Charting* **2021**, *41*, 61–64.
34. Yun, T.S.; Francisca, F.M.; Santamarina, J.C.; Rupple, C. Compressional and Shear Wave Velocities in Uncemented Sediment Containing Gas Hydrate. *Geophys. Res. Lett.* **2005**, *32*, 10. [CrossRef]
35. Lu, Y.; Meng, D.; Wang, L.; Weng, P. Recognition and Saturation Prediction of Gas Hydrates with Fracture Fill Characteristics. *Acta Geol. Sin.* **2024**, *98*, 2666–2677.
36. Chen, Y.; Dunn, K.-J.; Liu, X.; Du, M.; Lei, X. New Method for Estimating Gas Hydrate Saturation in the Shenhu Area. *Geophysics* **2014**, *79*, IM11–IM22. [CrossRef]

Disclaimer/Publisher's Note: The statements, opinions and data contained in all publications are solely those of the individual author(s) and contributor(s) and not of MDPI and/or the editor(s). MDPI and/or the editor(s) disclaim responsibility for any injury to people or property resulting from any ideas, methods, instructions or products referred to in the content.